Inorganic Chemistry Communications 159 (2024) 111854

Contents lists available at ScienceDirect

Inorganic Chemistry Communications

journal homepage: www.elsevier.com/locate/inoche

Short communication

Novel mesoporous iron oxide synthesized from naturally occurring magnetic sand: A potential and promising catalyst for chemical processes

Zaharaddeen Sani Gano *, Ephraim Akuaden Audu, Aisha Ayoola Osigbesan, Adebola Femi Ade-Ajayi, Jeffrey Tsware Barminas

National Research Institute for Chemical Technology, Basawa, Zaria, Kaduna State, Nigeria

ARTICLE INFO

Keywords:
Mesoporous
Magnetic sand
Iron oxide
Spectroscopy

ABSTRACT

This paper presents the synthesis of iron oxide from natural magnetic sand that was obtained from Michika, Adamawa State, Nigeria. Characterization of the raw magnetic sand and the synthesized iron oxide was performed to investigate the effect of the synthesis method on functional groups, morphology, composition, crystallinity, acidity and surface area/pore distribution using Fourier transform infrared (FTIR) spectroscopy, scanning electron microscopy – energy dispersive X-ray (SEM – EDX), X-ray fluorescence (XRF), X-ray diffraction (XRD), BET and pyridine FTIR, respectively. The XRF analysis of the two samples revealed a significant variation in oxide composition. The raw magnetic sand had an iron oxide content of 64.69 wt%, which increased to 85.20 wt% after synthesis. Furthermore, the SEM-EDX analysis indicated a decrease in average particle size from 114.6 and 36.8 μm for the respective samples. The XRD patterns revealed that the crystallinity increased after synthesis. FTIR showed the associations of functional groups present in the sample. The wavebands in the range 550 – 630 cm^{-1}, which correspond to the Fe – O bond, improved clearly in the synthesized iron oxide sample, particularly at 582 cm^{-1}. The pyridine FTIR depicts that the overall acidic site is higher in the synthesized sample. The N_2 adsorption–desorption procedure shows an increased BET surface area from 9.394 m^2/g (raw) to 24.851 m^2/g (synthesized). Overall, the results showed that the synthesized mesoporous iron oxide exhibits properties similar to materials that have a high potential for application as catalysts in chemical processes.

1. Introduction

Nigeria is endowed with enormous solid minerals identified in various locations across the country [1]. Some of these minerals include gold, iron ore, cassiterite, columbite, wolframite, pyrochlore, monazite, marble, coal, limestone, clays, barites, and lead–zinc. These minerals have played vital roles in chemical processes as active components or promoters in catalyst matrixes. However, at present, very few of these ores are being mined, processed and utilized for such purposes.

Many deposits of iron ore have been found in the country. The types of deposits discovered include haematite-magnetite, haematite-goethite and siderite-goethite [2]. These deposits are abundant in Kwara and Kogi States. Other states include Nasarawa, Adamawa, Sokoto, Kaduna, Oyo, Osun, Delta, Bauchi, Borno and Benue. This led to the establishment of Ajaokuta and Aladja iron and steel plants in Kogi and Delta States, respectively, to lay a formidable foundation for the technological advancement of steel rolling mills in the country [3]. However, its utilization has been mainly for smelting and construction, with little attention given to other applications [3,4].

In its naturally occurring state, iron ores have been used as catalysts in reactions such as Fenton oxidation in water treatment processes [5,6], reduction of NO with NH_3 [7], reforming of volatiles from the copyrolysis of lignite and corn straw [6] and tar decomposition [8,9]. In addition, iron-based catalysts have been used in Fischer-Tropsch synthesis for the production of fine chemicals, particularly olefins [10], the Haber process (ammonia synthesis) [11] and the upgrading of pyrolysis oil [12–14]. Iron-based catalysts have the advantage of being relatively cheap and possess low toxicity and high activity when used in numerous chemical reactions [10].

Most naturally occurring magnetic sands are considered low-grade iron oxide due to the high level of impurities that affect their porosity and purity. These problems underscore the need for a cost-effective and suitable method for the production of high-purity iron oxide from magnetic sand. Different techniques have been employed by researchers

* Corresponding author.
E-mail addresses: zaharaddeenn@gmail.com, zs.gano@narict.gov.ng (Z. Sani Gano).

https://doi.org/10.1016/j.inoche.2023.111854
Received 27 June 2023; Received in revised form 20 November 2023; Accepted 6 December 2023
Available online 9 December 2023

for the extraction/purification of iron oxide from these magnetic sands, such as sol–gel [15], coprecipitation [16], flame spray pyrolysis [17] and hydrothermal methods [18]. In the work of Shah, Ahmad [19], iron oxide nanoparticles were successfully synthesized from iron oxide-rich sand using the precipitation method, and approximately 76% iron was obtained. Salomo, Erwin [20] prepared iron oxide from natural sand obtained from the Rokan River, Indonesia, using the ball milling method and obtained a purity level of approximately 35% from approximately 2% Salomo, Erwin [20]. Maghemite, an iron III oxide, was synthesized by the coprecipitation method from natural sand obtained in a community in Singapore, as reported in the work of Cheng, Tan [21]. The analysis carried out in these works showed that the process of preparation is instrumental to the purity level of the obtained oxide, which invariably should increase substantially from a low concentration in the magnetic sand to a high concentration in the final product.

Literature have documented that most iron-based product and processes have been synthesized predominately using commercially available iron salts [21–23]. Currently, there has been no work reporting the synthesis of mesoporous iron oxide from naturally occurring magnetic sand. Moreover, the synthesis of such type of iron oxide for potential application for industrial processes represents a novel utilization of regional resources for sustainable processes. Exploring natural resources like iron oxide from naturally occurring magnetic sand for industrial applications will improve resource management, reduce over reliance on imported products, develop local processing industries and enhance economic benefits to the communities in Nigeria and West Africa at large where such types of materials are dominantly found.

The synthesis, characterization, and application of novel porous materials have been strongly encouraged due to the wide range of applications in adsorption, separation, catalysis, and sensors [24]. Mesoporous iron oxide and its supports have been shown to exhibit excellent performance as heterogeneous catalysts, which is attributed to their wide pore size (2–50 nm), large pore volume and high surface area [25]. A higher surface area enhances their capacity for chemical reactions/adsorption processes by providing more active sites. These compounds play a vital role in catalysis as well as other applications. The formation of well-defined pores within these materials could be affected by different factors, such as the synthesis method, reaction conditions and precursor material [26].

While previous research has explored the catalytic properties of magnetic sand impregnated with kaolin from Adamawa [27], the synthesis of mesoporous iron oxide from this magnetic sand remains unexplored. In this study, we employed an acid leaching-precipitation method to synthesize mesoporous iron oxide from raw magnetic sand from Michika, Adamawa State, Nigeria. This method offers several advantages, including ease of preparation, shorter synthesis time, lower reaction temperatures, products obtained are crystalline and homogeneous [28]. The resulting iron oxide was extensively characterized using various techniques and compared with raw magnetic sand to evaluate its mesoporosity, acidity and other structural properties.

This study addresses two crucial research questions: first, whether there is a difference in morphology and composition between the synthesized iron oxide and the raw magnetic sand and second, what is the effect of our synthesis method on the porosity, acidity and other catalytic properties of the synthesized iron oxide when compared to the raw magnetic sand. Therefore, this study aims to synthesize iron oxide from naturally occurring magnetic sand and characterize the product for potential application as a catalyst in chemical processes.

2. Experimental methodology

2.1. Equipment, materials and Reagents:

Weighing balance (Kern-EW6000, with an accuracy of 0.001 g), digital hotplate with a magnetic stirrer (Stuart CD 162), muffle furnace (SXL – 1008 Gallenkamp, England), vacuum pump, hot air oven (Genlab, UK), Gas mask, Wattman No. 1 Filter paper, Desiccator with a tap, Hydrochloric acid (Sigma Aldrich, 37%), Ammonium hydroxide (Sigma Aldrich, 33%), Pyridine (BDH Chemicals Limited UK, 99% analar grade), distilled water (Water Still Aquatton (A8000) Distiller). All reagents were used as supplied.

2.2. Synthesis of iron oxide

2.2.1. Sample preparation

Raw magnetic sand was dried for 4 h in an oven at a temperature of 120 ℃ to remove water content and then calcined at 800 °C in a muffle furnace for 3 h [29]. Thereafter, the calcined sample was crushed into a very fine powder using a ceramic mortar and pestle.

2.2.2. Leaching and precipitation of iron oxide from raw magnetic sand

The method of Bukit et al. [28] was used with slight modifications. The calcined sample was treated with 12 M HCl in a weight ratio of 1:2 (sample to acid) at 70 °C for 30 min on a hotplate with a magnetic stirrer at 300 rpm. The solution was filtered using a Buchner filtration setup.

Iron oxide was precipitated from the filtrate using an excess of 20% ammonium hydroxide (NH_4OH). NH_4OH was added dropwise to the filtrate while stirring on a hotplate with a magnetic stirrer at 70 °C in a fume hood until a darkish black precipitate was obtained. The precipitate was filtered and washed several times with distilled water to wash off chlorides and other impurities until a pH of 6.47 was achieved. Then, the washed precipitate was dried in an oven at 120 °C for 5 h and further calcined at 550 °C for 3 h. The calcined sample was thereafter crushed to a fine powder and packaged for subsequent analyses.

2.3. Characterization techniques

Infrared data were collected using a Shimadzu-8400S Fourier transform infrared spectrometer (Kyoto, Japan) over the range of 4000–400 cm^{-1}. X-ray diffraction (XRD) measurements were conducted to determine the crystallinity of the sample using an Empyrean Pan Analytical X-ray diffractometer (Worcestershire, United Kingdom) with 2θ between 2 and 80°. The elemental composition and morphology of the sample were determined to ascertain the percentage abundance of Fe in the sample using a Phenom world SEM-EDX analyser (Thermo Fischer. Waltham, U.S). BET surface area and porosity measurements were conducted using a Vsorb 2800P porosity analyser (GoldApp, China) at −196 °C after degassing for 7 h at 250 °C.

2.3.1. Acidity test using pyridine as a probe molecule

The method of Barzetti et al. [30] with slight modification was used for the acidity test. Briefly, 0.2 g of both raw magnetic sand (a) and synthesized iron oxide (b) were weighed in a small flat dish and placed in an oven for degassing at 200 °C for 2 h. The degassed samples were immediately placed in a desiccator containing pyridine at the bottom. The setup was then connected to a vacuum pump. The pump was turned on, and pyridine adsorption was allowed for 30 min. After the adsorption process, samples were quickly transferred into a second desiccator for stabilization. Thereafter, Fourier transform infrared spectroscopy (FT-IR) analysis was carried out on the samples using attenuated total reflectance (ATR) in the range of 1400 to 1700 cm^{-1}.

3. Results and discussion

3.1. Physical appearance of samples

The physical appearance of the raw magnetic sand was granulated and blackish. After extraction, precipitation, calcination and crushing of the sample, the product obtained was a fine reddish-brown powder, as shown in Fig. 1.

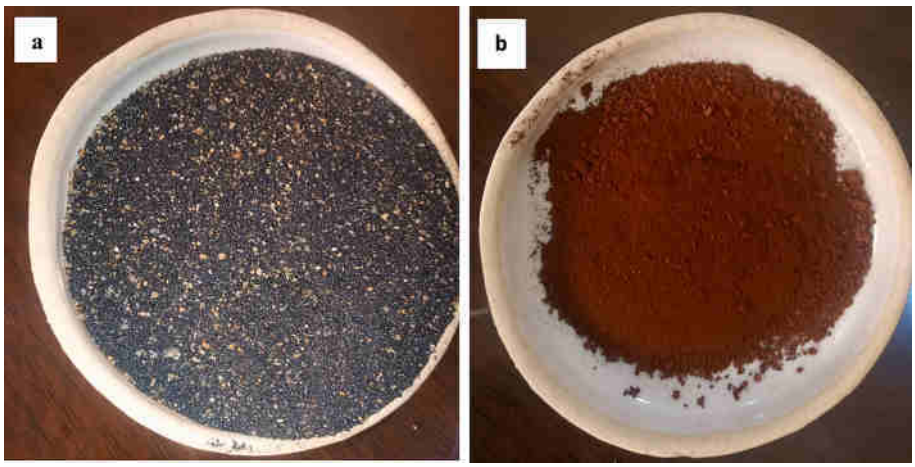

Fig. 1. Physical appearance of (a) raw magnetic sand and (b) synthesized iron oxide.

3.2. Characterization

3.2.1. Fourier transform infrared spectroscopy (FTIR) analysis

The FTIR spectra of the raw magnetic sand and the synthesized iron oxide are presented in Fig. 2. Each spectrum shows a similar pattern in energy bands, implying that the materials have similar functional groups. However, it was observed that the peaks in the synthesized iron oxide were more symmetrical with less noise, suggesting higher purity compared to the raw magnetic sand. The bands at 3404 cm^{-1} and 1643 cm^{-1} indicate an O–H stretching and bending vibration mode of adsorbed water that could have been attached to the surface iron atoms [31]. The peak is smaller in the synthesized iron oxide, suggesting that it contains less adsorbed water, thus implying enhanced purity. The IR absorption bands in the 550–630 cm^{-1} range correspond to the vibrations of Fe-O bonds in tetrahedral and octahedral sites, which are indicative of the formation of a spinel structure [32]. The band at 582 cm^{-1} is attributed to the Fe–O bond vibration of Fe_3O_4 in magnetite [33], while that found at 457 cm^{-1} denotes the Fe-O of maghemite [34]. These peaks are more prominent and symmetrical in the synthesized iron oxide, further indicating enrichment and purity of iron oxide when compared to the raw magnetic sand. The peak found at 1139 cm^{-1} suggests a Si-O stretching vibration [35].

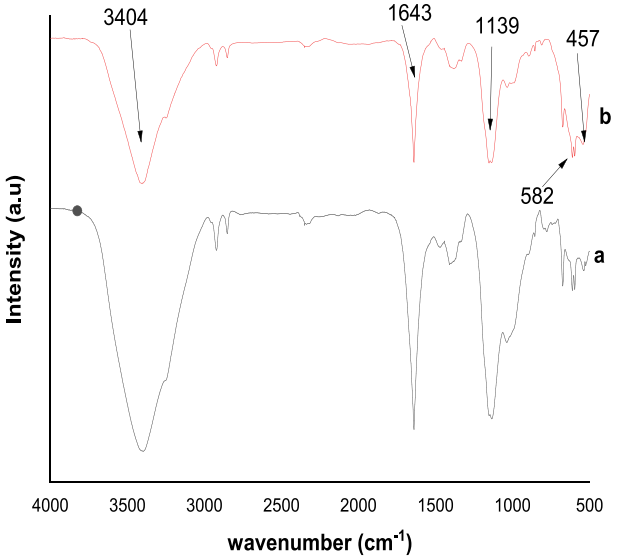

Fig. 2. FTIR spectra of (a) raw magnetic sand and (b) synthesized iron oxide.

3.2.2. Oxide composition and morphology analysis

The results obtained from the oxide analysis of the raw magnetic sand and synthesized iron oxide are shown in Table 1. The result shows that iron oxide (Fe_2O_3) is the major compound present in both samples. However, the Fe_2O_3 content increased from 64.69 wt% to 85.20 wt% after synthesis, which shows that the synthesis method extracted most of the iron oxide present in the raw magnetic sand. This value is in clear distinction from what was obtained by Salomo et al. (2020) and Shah et al. (2021). Furthermore, the concentration of other oxides found in the raw samples decreased significantly in the synthesized sample, signifying that the synthesis method is selective towards iron oxide purification. For instance, SiO_2, Al_2O_3, CaO and ZnO decreased from 17.67, 8.05, 1.39 and 0.04 wt% to 2.65, 5.13, 0.51 and 0.03 wt%, respectively. These findings are in agreement with the works of Chaki et al. (2015) who reported on the wet chemical reduction of magnetite using a similar method. Nonetheless, this work shows improved purity of iron oxide (85.20 wt%) compared to theirs (74.5 wt%) [36].

The SEM investigations further show the morphology of the samples at a magnification of 200 μm, as shown in Fig. 3. The images show that the magnetic sand appeared to have larger pseudospherical-sized particles, while the synthesized iron oxide had smaller particles. A particle size distribution histogram obtained from the analysed SEM data of both samples using ImageJ software is presented in Fig. 4. The particle size for the raw magnetic sand was found within the range of 40 – 200 μm with an average particle size of 114.6 μm. Similarly, the particle size for the synthesized Fe-O was found to be within 40–80 μm with an average particle size of 36.8 μm. This implies more surface area for a reaction when applied as a catalyst in chemical reactions. The size reduction may likely be a result of removed silicon compounds and other impurities, as

Table 1
Oxide composition (% weight) of raw magnetic sand and synthesized iron oxide obtained from XRF analysis.

Element	Raw (wt%)	Synthesized (wt%)
Fe_2O_3	64.69	85.20
MnO	0.25	0.17
CaO	1.39	0.51
SiO_2	17.67	2.65
Al_2O_3	8.05	5.13
P_2O_5	0.09	0.09
SO_3	0.05	0.72
V_2O_5	0.41	0.43
K_2O	0.55	0.04
Ag_2O	0.00	0.00
ZnO	0.04	0.03
CuO	0.01	0.04
TiO_2	5.391	0.27

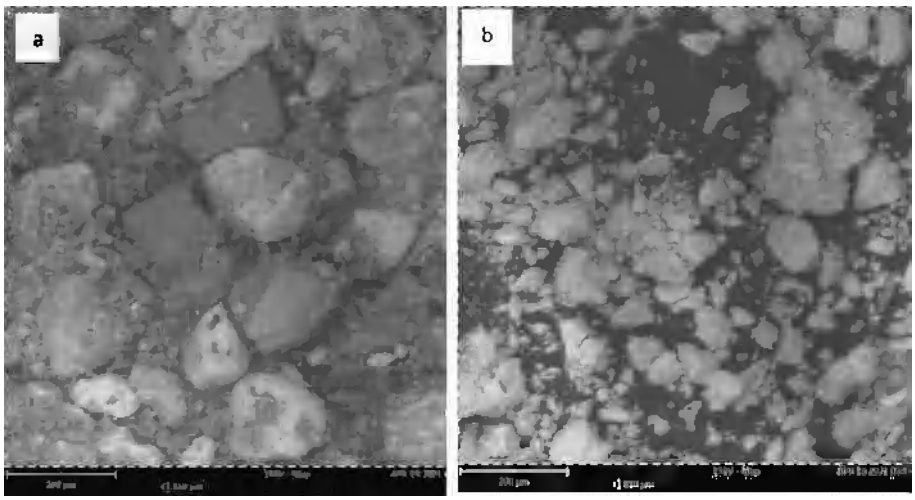

Fig. 3. Morphology at ×200 μm for (a) raw magnetic sand and (b) synthesized iron oxide.

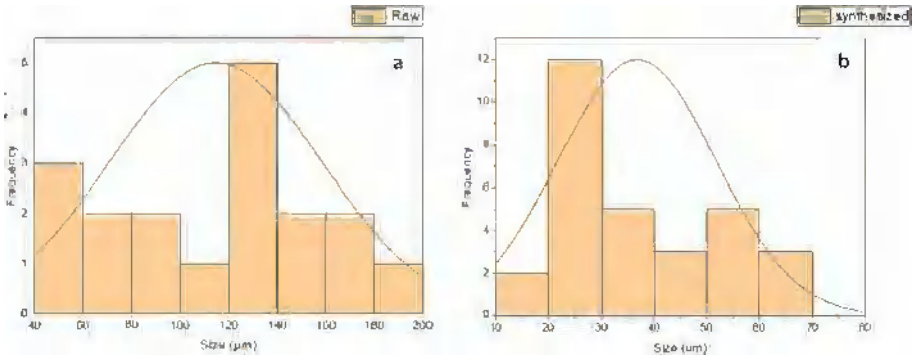

Fig. 4. Particle size distribution histogram of (a) raw magnetic sand and (b) synthesized iron oxide.

can be confirmed by the EDX shown in Fig. 5.

3.2.3. X-ray diffraction (XRD)

The XRD patterns of the raw magnetic sand and the synthesized iron oxide are presented in Fig. 6. The well-defined peaks in the patterns depict a high level of crystallinity in the samples.

The XRD results are further illustrated in Figs. 7 and 8 obtained from the analysis of the XRD spectra carried out using High Score Plus software (Version 3.0.4) from PANanalytical. Fig. 7 shows the patterns and prominence of magnetite (Fe_3O_4), quartz (SiO_2) and calcite ($CaCO_3$) in the analysed diffractograms of the raw magnetic sand, matching compounds in the Inorganic Crystal Structure Database (ICSD) with reference numbers 00–033-0664, 00–046-1045 and 00–005-0586, respectively.

The peaks peculiar to Fe_3O_4 are located at 2theta = 24.0, 30.2, 35.5, 43.3, 49.4, 57.2, 62.7 and 71.5°. The peaks associated with SiO_2 are at 2theta = 20.9, 26.8, 36.6, 45.9, 50.9, 55.5, 60.1, 67.7°, while those associated with $CaCO_3$ are located at 2theta = 23.4, 29.9, 36.6, 39.3, 43.5, 48.9, 57.2, 61.2 and 63.3°.

Fig. 8 describes the patterns and prominence of the compounds detected by XRD in the synthesized iron oxide. The analysis of the result by the same software shows an improvement in the composition of the iron oxide. It was observed that the peaks of iron oxide (Fe_2O_3) are more prominent than those of other detected compounds. These peaks are found at 2 theta = 24.3, 33.0, 35.3, 41.1, 49.4, 54.1, 57.6, 62.4, 63.9, 71.9 and 75.4°.

The analysis of both samples describes the crystal shapes as rhombohedral for the compounds found in the magnetic sand except for quartz, which is described as hexagonal, while the crystal shape is generally rhombohedral in the synthesized iron oxide as a result of the synthesis.

3.2.4. Surface area and porosity analysis

The adsorption isotherms of nitrogen at 77 K and the corresponding BJH pore size distribution are illustrated in Fig. 9a and 9b and Table 2. The isotherm of raw magnetic sand (9a) can be related to a type III adsorption isotherm [37], with characteristic weak pores in the material. This feature of the material is highly undesirable, particularly for

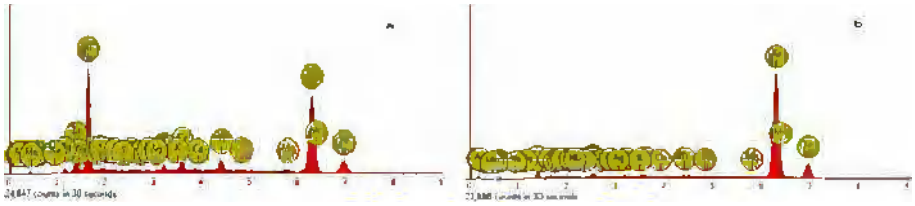

Fig. 5. EDX of (a) raw magnetic sand and (b) synthesized iron oxide.

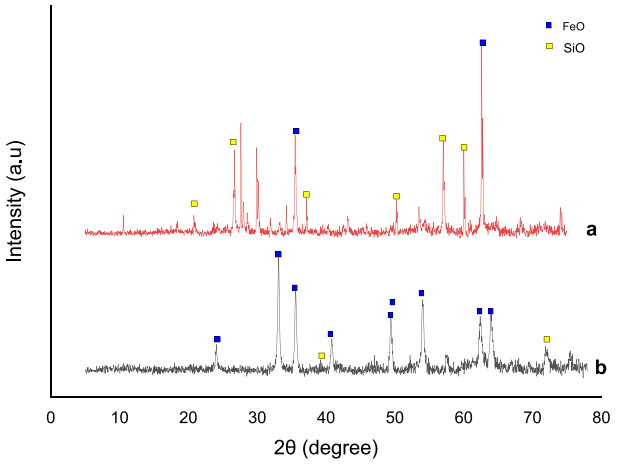

Fig. 6. XRD patterns of (a) raw magnetic sand and (b) synthesized iron oxide.

application in catalyst development. However, the isotherm profile of the synthesized iron oxide (9b) can be related to type IV, with a typical hysteresis loop of mesoporous materials. This is usually associated with capillary condensation of adsorbed gas (nitrogen) taking place in the pores of the sample [38].

The improvement in mesoporosity noticed in the synthesized iron oxide sample can be confirmed by the BJH pore size distributions shown in Table 2. Both samples exhibit pore widths above 2 nm, an indication that they are mesoporous materials [36,39,40]. However, the synthesized iron oxide shows a smaller pore width (2.502 nm), suggesting that the synthesized iron oxide is more mesoporous than the raw magnetic sand [41]. Similarly, the surface area increased from 9.394 m^2/g for raw magnetic sand to 24.851 m^2/g for the synthesized iron oxide. The BJH pore volume increased from 0.014 cm^3 for the raw magnetic sand to 0.050 cm^3/g for the synthesized iron oxide, which is beneficial for chemical processes such as adsorption [18]. This analysis shows a clear effect of the synthesis process on the magnetic sand.

3.2.5. Acidity test

Pyridine FTIR was carried out to detect the acidity of the samples both before and after synthesis. Acidity is usually confirmed by the presence of Lewis acid (LA) and Bronsted acid (BA) sites in the samples [42]. Pyridine acts as a probe molecule for the quantification and detection of Bronsted and Lewis acidic sites present in the catalyst pore spacing. The interaction of pyridine vapour and the sample results in bond formation by the lone pair present in pyridine with the proton available in the catalyst via different routes: The nitrogen lone pair present in pyridine can interact weakly with a hydroxyl group on the

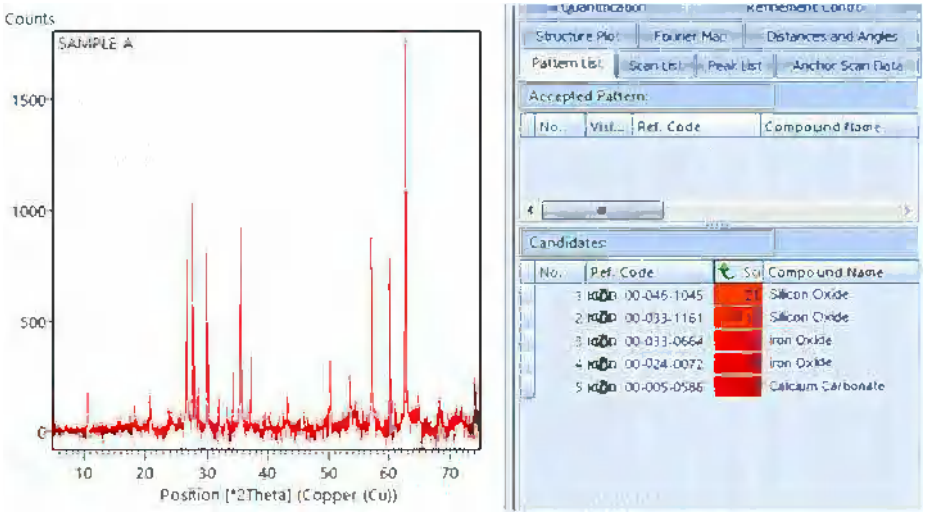

Fig. 7. XRD pattern of the raw magnetic sand showing the prominent compounds.

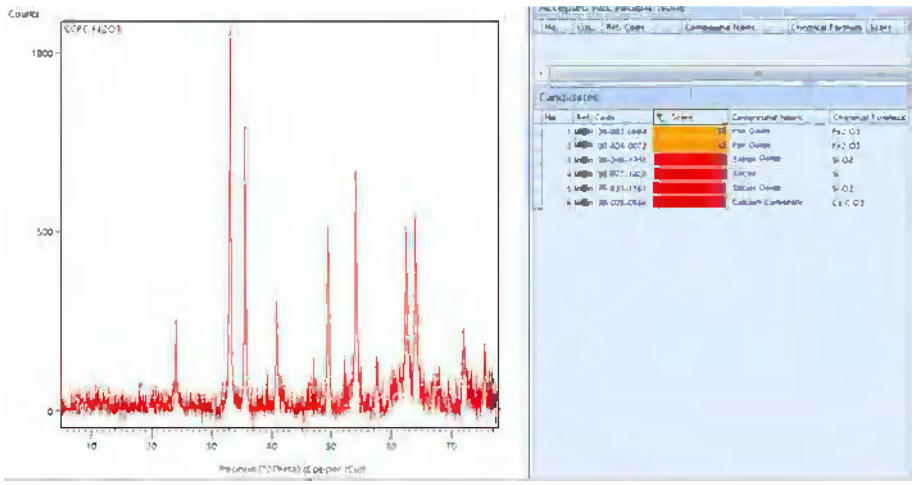

Fig. 8. XRD pattern of the synthesized iron oxide with the most prominent compound.

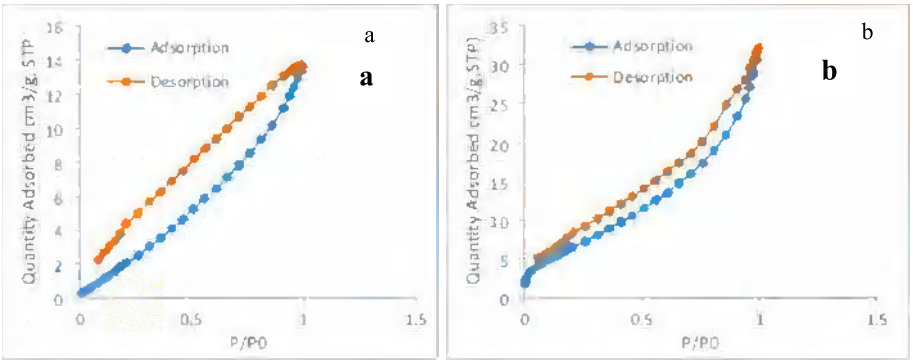

Fig. 9. Adsorption isotherms for (a) raw magnetic sand and (b) synthesized iron oxide.

Table 2
Surface area and porosity measurements of raw and synthesized magnetic sand.

Parameter	Raw (a)	Synthesized (b)
BET surface area (m^2/g)	9.394	24.851
BJH median pore width (nm)	3.114	2.502
BJH Pore volume (cm^3/g)	0.014	0.050

surface of the catalyst to form a hydrogen bond, interact with a Bronsted acidic site to form a pyridinium ion by transfer of a proton from the catalyst surface to pyridine, or the lone pair could interact by donating an electron to the unsaturated cation coordinated to a Lewis acidic site [42].

Figs. 10 and 11 show the spectra of pyridine FTIR before and after pyridine adsorption on the raw magnetic sand and the synthesized iron oxide, respectively. It can be seen from the spectra that three (3) distinctive peaks, which are common to pyridine adsorption, were noticed at 1421, 1535 and 1624 cm^{-1}. The peaks located at 1535 cm^{-1} suggest a characteristic adsorption peak that corresponds to a 19a vibration mode ascribed to pyridinium ions adsorbed on Brønsted sites [43]. Meanwhile, the peak located at 1642 cm^{-1} depicts an 8a vibration mode of pyridine coordinated protons on Lewis sites [42,44]. The peak found at 1448 cm^{-1} could be assigned to pyridine and silanol groups associated via a hydrogen bond [45].

A general comparison of all the spectra shows that the Lewis acidic sites were more prominent with higher intensity than the Bronsted acid sites. This observation suggests that the sample is dominated by Lewis

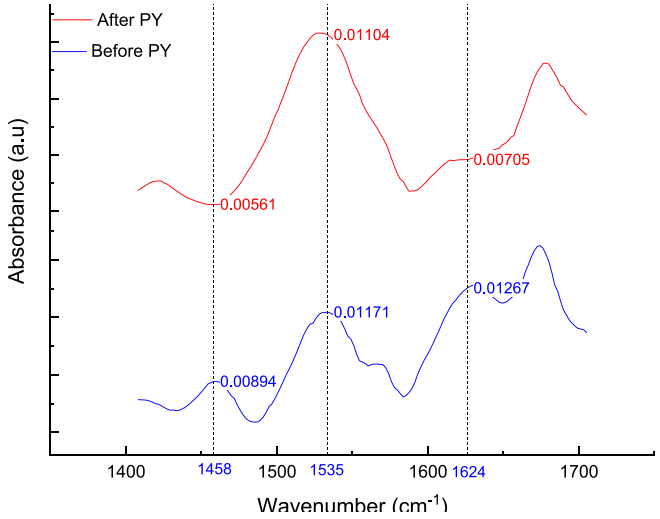

Fig. 10. FTIR (ATR) spectra of raw magnetic sand before and after pyridine adsorption.

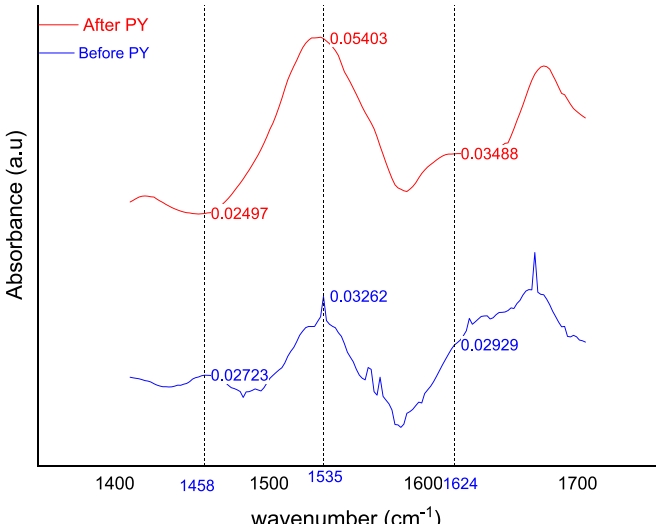

Fig. 11. FTIR (ATR) spectra of synthesized iron oxide before and after pyridine adsorption.

acidic sites. Research carried out by Maronna et al. (2016) [45] showed that Lewis acidic sites were enhanced by the addition of Fe onto a catalyst. Additionally, it is worth noting that the overall acidic sites were more pronounced on the synthesized iron oxide than on the raw magnetic sand, which is evident by the increase in absorbance intensity of the acid sites in the synthesized iron oxide (0.054 LA and 0.035 BA absorbance value) when compared with the raw magnetic sand (0.011 LA and 0.007 BA absorbance value). Moreover, the area of absorption for the acidic sites for the synthesized iron oxide was higher than that in the raw sample. These observations show that the synthesis process of iron oxide from magnetic sand enhances the surface chemistry, porosity and surface area of the sample, which increases the number of acidic sites in the sample. According to Mukhamatdinov et al. (2020) [46], iron-based catalysts provide suitable active sites for the cracking of carbon–carbon bonds, leading to the formation of smaller hydrocarbon fragments (saturates and aromatics) suitable for fuel production. The effect of impurities on acidity or catalytic activity is apparent from the presented results. The removal of volatile organic compounds and other impurities present in the raw magnetic sand resulted in the enrichment of acidic sites on the surface of the synthesized mesoporous iron oxide. These impurities could have been occupying the active sites in the mesopores of the raw sample. Furthermore, the synthesis process increased the surface area and enhanced the mesoporosity of the sample, resulting in a higher number of active sites on the material surface, including acidic sites. Lewis and Bronsted acidic sites on catalyst surfaces activate reactants by introducing a positive charge, thereby enhancing the reactivity by lowering the activation energy of the

initiation step that leads to product formation [43].

4. Conclusion

Iron oxide was synthesized using an acid leaching-precipitation method from locally sourced magnetic sand. The data from the XRF analysis showed that the iron content from the magnetic sand increased from 64.69 to 85.20 wt%, while the average particle size decreased from 114.6 to 36.8 μm after synthesis. The XRD results obtained confirmed the crystallinity of the synthesized sample. The results from the BET surface area analysis showed that the magnetic sand is inherently mesoporous; however, the pore analysis on the two samples showed that the porosity of the synthesized iron oxide has improved, thereby making it more mesoporous with a larger surface area and pore volume over the raw magnetic sand. The results obtained from the acidity test showed that acidity was enhanced with more acidic sites in the synthesized sample. All these findings point to the fact that the synthesized sample exhibits properties that qualify it for application as a catalyst in chemical processes.

CRediT authorship contribution statement

Zaharaddeen Sani Gano: Conceptualization, Project administration, Writing – review & editing. **Ephraim Akuaden Audu:** Writing – original draft, Visualization, Methodology. **Aisha Ayoola Osigbesan:** Methodology, Writing – original draft. **Adebola Femi Ade-Ajayi:** Methodology, Writing – original draft. **Jeffrey T. Barminas:** Funding acquisition, Project administration, Supervision.

Declaration of Competing Interest

The authors declare that they have no known competing financial interests or personal relationships that could have appeared to influence the work reported in this paper.

Data availability

Data will be made available on request.

Acknowledgement

The authors appreciate the National Research Institute for Chemical Technology (NARICT) for the financial and technical support rendered in carrying out this research under the project number FGN/AB2021/ERGP30122610.

References

[1] U.A. Lar, Geology and mineral resources of Nigeria and their uses. in Paper presented, 2018.
[2] U.S. Bamalli, A. Moumouni, M.S. Chaanda, A review of Nigerian metallic minerals for technological development, Nat. Resour. 2 (2) (2011) 87.
[3] O.J. Kolawole, A.A. Akanni, B.S. Ameenullahi, A.A. Adediran, Preliminary characterisation of iron ores for steel making processes, Procedia Manuf. 35 (2019) 1123–1128.
[4] A. Biswas, Principles of Blast Furnace Iron Making, Calcutta, SBA Publications, India, 2005.
[5] T. de Melo Augusto, et al., Iron ore tailings as catalysts for oxidation of the drug paracetamol and dyes by heterogeneous Fenton, J. Environ. Chem. Eng. 6 (5) (2018) 6545–6553.
[6] H. Zhao, et al., Catalytic reforming of volatiles from co-pyrolysis of lignite blended with corn straw over three iron ores: Effect of iron ore types on the product distribution, carbon-deposited iron ore reactivity and its mechanism, Fuel 286 (2021), 119398.
[7] W. Chen, et al., In-situ DRIFTS investigation on the selective catalytic reduction of NO with NH3 over the sintered ore catalyst, Appl. Surf. Sci. 439 (2018) 75–81.
[8] A. Kurniawan, K. Abe, T. Nomura, T. Akiyama, Integrated pyrolysis–tar decomposition over low-grade iron ore for ironmaking applications: effects of coal–biomass fuel blending, Energy Fuel 32 (1) (2018) 396–405.
[9] R.B. Cahyono, M. Hidayat, T. Akiyama, Tar decomposition over porous low-grade iron ore, in: AIP Conference Proceedings. 2018. AIP Publishing LLC.
[10] L. Quiambao, A Scope on the Advantages and Limitations of Iron Catalysts in the Synthesis of Secondary Alcohols, UC Merced Undergraduate Res. J. 8 (1) (2015).
[11] B. Coşkuner Filiz, A. Kantürk Figen, Earth Abundant Catalysis for Ammonia Synthesis, in: in Sustainable Ammonia Production, Springer, 2020, pp. 1–16.
[12] S. Cheng, et al., Upgrading pyrolysis bio-oil to hydrocarbon enriched biofuel over bifunctional Fe-Ni/HZSM-5 catalyst in supercritical methanol, Fuel Process. Technol. 167 (2017) 117–126.
[13] A. Palizdar, S. Sadrameli, Catalytic upgrading of beech wood pyrolysis oil over iron-and zinc-promoted hierarchical MFI zeolites, Fuel 264 (2020), 116813.
[14] S. Cheng, L. Wei, J. Julson, M. Rabnawaz, Upgrading pyrolysis bio-oil through hydrodeoxygenation (HDO) using non-sulfided Fe-Co/SiO2 catalyst, Energ. Conver. Manage. 150 (2017) 331–342.
[15] A.E. Gash, et al., Use of epoxides in the sol– gel synthesis of porous iron (III) oxide monoliths from Fe (III) salts, Chem. Mater. 13 (3) (2001) 999–1007.
[16] R. Valenzuela, et al., Influence of stirring velocity on the synthesis of magnetite nanoparticles (Fe3O4) by the co-precipitation method, J. Alloy. Compd. 488 (1) (2009) 227–231.
[17] R. Strobel, S.E. Pratsinis, Direct synthesis of maghemite, magnetite and wustite nanoparticles by flame spray pyrolysis, Adv. Powder Technol. 20 (2) (2009) 190–194.
[18] A. Lassoued, et al., Synthesis, photoluminescence and Magnetic properties of iron oxide (α-Fe2O3) nanoparticles through precipitation or hydrothermal methods, Phys. E. 101 (2018) 212–219.
[19] N. Shah, et al., Synthesis and Characterization of Agar Coated Magnetic Iron Oxide Nanoparticles Prepared from Sand as Natural Iron Source for Removal of Ni ion from Aqueous, Solution. (2021).
[20] S. Salomo, et al., Preparation of Iron Oxide Magnetic Nanoparticles Natural Sand of Rokan River Synthesis with Ball Milling. Journal of Physics: Conference Series, IOP Publishing, 2020.
[21] Z. Cheng, et al., Synthesis and characterization of iron oxide nanoparticles and applications in the removal of heavy metals from industrial wastewater, Int. J. Photoenergy 2012 (2012).
[22] S. Natarajan, et al., Multifunctional magnetic iron oxide nanoparticles: Diverse synthetic approaches, surface modifications, cytotoxicity towards biomedical and industrial applications, BMC Materials 1 (1) (2019) 1–22.
[23] M. Farahmandjou, A. Khodadadi, M. Yaghoubi, Low Concentration Iron-Doped Alumina (Fe/Al 2 O 3) Nanoparticles Using Co-Precipitation Method, J. Supercond. Nov. Magn. 33 (2020) 3425–3432.
[24] Z.A. ALOthman, A review: fundamental aspects of silicate mesoporous materials, Materials 5 (12) (2012) 2874–2902.
[25] M. Zhou, et al., Solvent-free and rapid synthesis of mesoporous Pt–iron oxide catalysts via mechanochemical assembly, Cat. Sci. Technol. 9 (15) (2019) 3907–3913.
[26] D. Wang, W. Yang, S. Feng, H. Liu, Constructing hybrid porous polymers from cubic octavinylsilsequioxane and planar halogenated benzene, Polym. Chem. 5 (11) (2014) 3634–3642.
[27] M. Iji, P.M. Dass, K.W. Shalbugau, B.L. Penuel, Synthesis and Characterization of Heterogeneous Catalysts from Magnetic Sand and Kaolin, J. Chem. Lett. 1 (3) (2020) 139–142.
[28] N. Bukit, E. Frida, P. Simamora, T. Sinaga, Synthesis Of Fe3O4 nanoparticles of iron sand coprecipitation method with polyethylene glycol 6000, J. Chem. Mater. Res. 7 (07) (2015) 110–115.
[29] A. López-Vásquez, A. Suárez-Escobar, J.H. Ramírez, Effect of calcination temperature on the photocatalytic activity of nanostructures synthesized by hydrothermal method from black mineral sand, ChemistrySelect 5 (1) (2020) 252–259.
[30] T. Barzetti, E. Selli, D. Moscotti, L. Forni, Pyridine and ammonia as probes for FTIR analysis of solid acid catalysts, J. Chem. Soc. Faraday Trans. 92 (8) (1996) 1401–1407.
[31] W. Cai, J. Wan, Facile synthesis of superparamagnetic magnetite nanoparticles in liquid polyols, J. Colloid Interface Sci. 305 (2) (2007) 366–370.
[32] S.J. Iyengar, et al., Magnetic, X-ray and Mössbauer studies on magnetite/maghemite core–shell nanostructures fabricated through an aqueous route, RSC Adv. 4 (110) (2014) 64919–64929.
[33] A. Maharramov, et al., The synthesis and coupling with magnetite nanoparticles oF 4, 6-dimethyl-2-(2-oxyethyl)-1, 2-dihydro-3H-pyrrolo [3, 4-C] pyridine-3-one and characterization its structure, J. Optoelectron. Biomed. Mater. 8 (4) (2016) 169–174.
[34] D.D. Suppiah, S.B. Abd Hamid, One step facile synthesis of ferromagnetic magnetite nanoparticles, J. Magn. Magn. Mater. 414 (2016) 204–208.
[35] K. Rajkumari, J. Kalita, D. Das, L. Rokhum, Magnetic Fe 3 O 4@ silica sulfuric acid nanoparticles promoted regioselective protection/deprotection of alcohols with dihydropyran under solvent-free conditions, RSC Adv. 7 (89) (2017) 56559–56565.
[36] S.H. Chaki, et al., Magnetite Fe 3 O 4 nanoparticles synthesis by wet chemical reduction and their characterization, Adv. Nat. Sci. Nanosci. Nanotechnol. 6 (3) (2015), 035009.
[37] S. Kumar, M. Kumar, A. Singh, Synthesis and characterization of iron oxide nanoparticles (Fe2O3, Fe3O4): a brief review, Contemp. Phys. 62 (3) (2021) 144–164.
[38] L. Macera, et al., Nano-sized Fe (III) oxide particles starting from an innovative and eco-friendly synthesis method, Nanomaterials 10 (2) (2020) 323.
[39] S. Lowell, J.E. Shields, M.A. Thomas, M. Thommes, Characterization of Porous Solids and Powders: Surface Area, Pore Size and Density, 2006.
[40] M. Waseem, S. Munsif, U. Rashid, D. Imad ud, Physical properties of α-Fe2O3 nanoparticles fabricated by modified hydrolysis technique, Appl. Nanosci. 4 (5) (2014) 643–648.

[41] S. Fu, et al., Accurate characterization of full pore size distribution of tight sandstones by low-temperature nitrogen gas adsorption and high-pressure mercury intrusion combination method, Energy Sci. Eng. 9 (1) (2021) 80–100.
[42] A. Penkova, et al., Pyridine adsorption on NiSn/MgO–Al2O3: An FTIR spectroscopic study of surface acidity, Appl. Surf. Sci. 317 (2014) 241–251.
[43] K. Cheng, et al., Enhancing the low temperature NH 3-SCR activity of FeTiO x catalysts via Cu doping: a combination of experimental and theoretical study, RSC Adv. 8 (34) (2018) 19301–19309.
[44] M.I. Zaki, M.A. Hasan, F.A. Al-Sagheer, L. Pasupulety, In situ FTIR spectra of pyridine adsorbed on SiO2–Al2O3, TiO2, ZrO2 and CeO2: general considerations for the identification of acid sites on surfaces of finely divided metal oxides, Colloids Surf A Physicochem Eng Asp 190 (3) (2001) 261–274.
[45] M. Maronna, et al., Spectroscopic study on the active site of a SiO 2 supported niobia catalyst used for the gas-phase Beckmann rearrangement of cyclohexanone oxime to ε-caprolactam, PCCP 18 (32) (2016) 22636–22646.
[46] I.I. Mukhamatdinov, et al., The composition and structure of ultra-dispersed mixed oxide (Ii, iii) particles and their influence on in-situ conversion of heavy oil, Catalysts 10 (1) (2020) 114.

ACADÉMIE
DES SCIENCES
INSTITUT DE FRANCE

Comptes Rendus
Chimie

Ephraim Akuaden Audu, Adebola Femi Ade-Ajayi, Aisha Ayoola Osigbesan, Zaharaddeen Sani Gano and Jeffrey Tsware Barminas

FeO–alumina catalyst for reforming waste polyethylene terephthalate (PET) pyrolyzed products: synthesis, characterization, and performance evaluation

Published online: 7 November 2024

Part of Special Issue: Materials and Energy Valorization of Biomass and Waste: The Path for Sustainability and Circular Economy Promotion

Guest editors: Mejdi Jeguirim (Université de Haute-Alsace, Institut de Sciences des Matériaux de Mulhouse, France) and Salah Jellali (Sultan Qaboos University, Oman)

https://doi.org/10.5802/crchim.343

The Comptes Rendus. Chimie *are a member of the Mersenne Center for open scientific publishing*
www.centre-mersenne.org — e-ISSN : 1878-1543

ACADÉMIE DES SCIENCES
INSTITUT DE FRANCE

Comptes Rendus. Chimie
Published online: 7 November 2024
https://doi.org/10.5802/crchim.343

Research article

Materials and Energy Valorization of Biomass and Waste: The Path for Sustainability and Circular Economy Promotion

FeO–alumina catalyst for reforming waste polyethylene terephthalate (PET) pyrolyzed products: synthesis, characterization, and performance evaluation

Ephraim Akuaden Audu [*,a], **Adebola Femi Ade-Ajayi** [a], **Aisha Ayoola Osigbesan** [a], **Zaharaddeen Sani Gano** [a] **and Jeffrey Tsware Barminas** [a]

[a] National Research Institute for Chemical Technology, Basawa, Zaria, Kaduna State, Nigeria

E-mails: akuadenaudu@gmail.com, ephraim.audu@narict.gov.ng (E. A. Audu)

Abstract. The growing rate of plastic pollution in Nigeria and across the globe, coupled with the need to harness such waste for useful purposes, is a pressing global concern. In this study, a new type of catalyst was synthesized by incorporating mesoporous FeO onto aluminium oxide trihydrate (alumina) and applied in reforming polyethylene terephthalate (PET) pyrolyzed gas into valuable fuels. The pyrolysis process was carried out at 500 °C while vapor reforming was carried out using 0.5 g of catalyst loading in a fixed bed reactor at 450 °C for 90 min. Scanning electron microscopy analysis of catalysts revealed particle sizes of 1.42–7.63, 1.37–10.75, and 2.66–6.34 μm for alumina, 3% FeO/Al, and 5% FeO/Al, respectively. The percentage compositions of Fe in the synthesized catalyst from the X-ray fluorescence results were found to be 4.7% and 3.62% for 5% FeO/Al and 3% FeO/Al, respectively. XRD analysis revealed that the synthesized catalysts were non-crystalline. Catalyst performance evaluation from the gaseous product revealed a decrease in oxygen from 23.3% in the blank run to 5.33% in 5% FeO/Al. The H_2 content was found to be highest in 5% FeO/Al with a value of 17.14% while the CH_4 content was found highest in 3% FeO/Al (16.22%). Fourier transform infrared analysis of the liquid products inferred peaks corresponding to aromatic and saturated hydrocarbons, which was confirmed by gas chromatography mass spectrometry analysis. Findings from this research demonstrated that the synthesized catalyst was able to reform waste PET pyrolyzed gas into valuable products, addressing environmental challenges and providing alternative energy sources.

Keywords. Catalyst, FeO, Polyethylene terephthalate, Pyrolysis, Reforming, Plastic waste.

Funding. National Research Institute for Chemical Technology (NARICT) under project number FGN/AB2021/ERGP30122610.

Manuscript received 4 March 2024, revised 6 June 2024 and 17 July 2024, accepted 17 September 2024.

1. Introduction

The increasing global production and use of plastics, such as polyethylene terephthalate (PET), polyethylene (PE), polystyrene (PS), and others, have led to growing concern about environmental pollution and waste management. Nigeria is the most populous country in Africa, located at the west African subregion. It holds a land area of 932,768 km^2

* Corresponding author

with an estimated population of 211.4 million [1]. According to Sogbanmu [2], Nigeria ranks ninth globally among countries with the highest contributions to plastic pollution, producing 2.5 million tons of plastic waste annually [3]. Furthermore, over 88% of the plastic waste generated is not recycled, suggesting that such waste is not properly managed. Currently, most plastic waste in the country is dumped at sites and landfills or incinerated. Improper disposal of plastic waste can lead to the leaching of toxic additives into water bodies, blocking of drainages, generation of microplastics, air pollution, and the release of greenhouse gases [4,5]. To achieve the United Nations Sustainable Development Goals (UN SDGs) by 2030, it is crucial to evaluate policy actions and programs at state, national, and regional levels to address plastic pollution [6].

PET has been used in many applications such as in bottles for beverages and water and packaging materials for foods and textiles [4,7,8]. However, the use of PET poses significant challenges due to its non-biodegradability, thereby leading to the generation of accumulated plastic waste. Consequently, finding sustainable and environmentally friendly methods for proper management of such waste is imperative.

Several conventional methods for plastic waste management have been considered; however, most of these methods have limitations. For instance, recycling plastic waste, which involves melting thermoplastics and remolding it to other products, is not sustainable due to the low-quality products produced [9]. Burning plastics in incinerators is another method of plastic waste management. Nevertheless, this method suffers several limitations, including generating greenhouse gases (CO_2, CH_4), air pollution, soil contamination, and even posing a threat to human health. Pyrolysis, as a plastic waste management method, offers promising solutions to address the limitations faced by other conventional methods [10,11]. Pyrolysis of plastic waste aligns with SDG 12, which aims to ensure sustainable consumption and production patterns by turning plastic waste into valuable resources. It offers the advantage of converting waste to valuable products such as fuels and other chemical feedstock, minimal environmental impact, job creation, renewable energy production, carbon sequestration, and promoting a circular economy [12,13].

Pyrolysis is a process of breaking down long-chain hydrocarbons into smaller chains with the application of heat and pressure in the absence of oxygen, leading to the formation of valuable products like gases, pyrolysis oils, and char [14]. The liquid oil can be further upgraded to produce fuels (gasoline, C5–C12 and diesel, C13–C20), lubricants, and other valuable chemicals [15]. Typically, pyrolysis involves heating the feedstock to a high temperature range between 400 and 800 °C, resulting in the rupturing of chemical bonds in the feedstock and formation of smaller molecules [16,17]. Pyrolysis is categorized into slow, fast, and flash pyrolysis based on the residence times and heating rates resulting in different product yields and compositions [18,19].

Several studies have been conducted on the pyrolysis of PET, which have shown that it contains saturates and aromatic compounds similar to those found in crude oil. For example, Xue et al. [20] carried out pyrolysis of plastics including PET using zeolite catalyst and found that aromatic hydrocarbons were the major products (52.71%) with lower yields of saturates (alkanes and alkenes). In another study, Du et al. [21] showed that aromatic hydrocarbons (mostly benzene) were obtained during the pyrolysis of PET carpet waste with ZSM-5 and CaO catalysts to enhance deoxygenation of the products. Suriapparao et al. [22] investigated the co-pyrolysis of PET with rice husk and found that it promoted the formation of aromatic oxygenates and biphenyl hydrocarbons. However, the major components obtained in microwave pyrolysis of PET were aromatics. The study also revealed that PET pyrolysis oil contains impurities, tars, a wide distribution of hydrocarbons, and oxygenated compounds, necessitating the need for upgrading such oils using suitable catalysts.

It has been reported that the use of acidic catalysts can aid in cracking and aromatization reactions during the pyrolysis of plastics [23,24]. Additionally, the use of catalysts can decrease the reaction temperature, shorten the reaction time, and reduce the formation of unwanted byproducts [25,26]. Supported iron catalysts have emerged as a promising option for PET pyrolysis, as literature has reported their enhanced efficiency, low cost, and selectivity during the pyrolysis process [27,28].

Although prior works have reported the synthesis of iron–alumina based catalysts [29–32], none have reported the synthesis of iron–alumina based

catalysts from mesoporous FeO derived from natural magnetic sand available locally in Nigeria. Moreover, no work has reported the use of such a catalyst for reforming PET pyrolysis vapor. In this study, a new type of catalyst was developed based on the combination of a novel mesoporous iron oxide synthesized from natural magnetic sand with alumina. The synthesized catalyst was then used to upgrade PET pyrolysis gas into valuable fuels. This study aims to answer the following research questions: first, how does the synthesized catalysts affect the distribution of pyrolysis products of PET after reforming; second, the effect of 3% and 5% FeO catalyst loading on selectivity. The findings of this study will contribute to the development of innovative catalysts and environmentally friendly approaches for PET pyrolysis into valuable fuels.

2. Materials and methods

2.1. *Material and equipment*

PET was obtained from used drinking water bottles within Zaria, Kaduna State. Prior to the experiment, PET bottle samples were cut into smaller pieces (average size within 2 cm × 2 cm) and allowed to dry in the laboratory. Aluminum oxide trihydrate (alumina) was purchased from Suffolk, England. Iron oxide (prepared from magnetic sand), weighing balance (Kern-EW6000, with an accuracy of 0.001 g), digital hotplate with a magnetic stirrer (Stuart CD162), muffle furnace (SXL-1008 Gallenkamp, England), vacuum pump, hot air oven (Genlab, UK), gas mask, Whatman No. 1 filter paper, distilled water (Water Still Aquatron [A8000] Distiller), and Infrared Syngas Analyzer Gasboard-3100P (Hubei Cubic-Ruiyi Instrument) were utilized. All reagents were used as supplied.

2.2. *Catalyst preparation*

Mesoporous FeO was incorporated into alumina through the incipient wetness impregnation technique to synthesize 3% and 5% FeO loaded on alumina (3% and 5% FeO/Al). The mesoporous FeO synthesized from magnetic sand according to the method of Gano et al. [33] was used to prepare 3% and 5% FeO precursor solution. The predetermined volume of precursor solutions, which is equivalent to the pore volume of the alumina, was then carefully added to the support. The mixture was continuously mixed until a homogeneous reddish-brown paste was obtained. The paste was oven-dried at 105 °C overnight, after which it was calcined in a muffle furnace for 3 h at 500 °C.

Figure 1. Multifunctional pyrolysis and fixed bed reactor system at NARICT, Zaria.

2.3. *Pyrolysis process*

PET pyrolysis was conducted using a multifunctional pyrolysis reactor system (PRS) at the National Research Institute for Chemical Technology (NARICT), Zaria (Figure 1). The PRS consisted of a pyrolyzer and fixed bed reactor (FBR; stainless steel tube, 40 cm length, 1 cm internal diameter; Figure 2). Initially, 200 g of PET was charged into the pyrolyzer followed by the passage of nitrogen gas at 0.5 bar for 1 h to create an inert environment. Pyrolysis was then carried out at 350 °C until the pressure in the pyrolyzer reached 10 bar.

While the pyrolyzer pressure was building up, 0.5 g of the catalyst was loaded in between glass wool plug beds inside the FBR. Prior to the start of the catalytic reforming process, N_2 gas was allowed to flow through the reactor at 0.5 bar for 15 min. Subsequently, the catalyst was reduced under H_2 flow at 0.5 bar and 450 °C for 90 min. When the pressure in the pyrolyzer is 10 bar, the bypass valves are opened to allow the pyrolysis vapor to contact the catalyst at 450 °C. At the end of the catalytic reforming process, the product was passed through a condenser into a liquid gas separator tank, where the condensable product is collected while the non-condensable product is directed to an online syngas analyzer

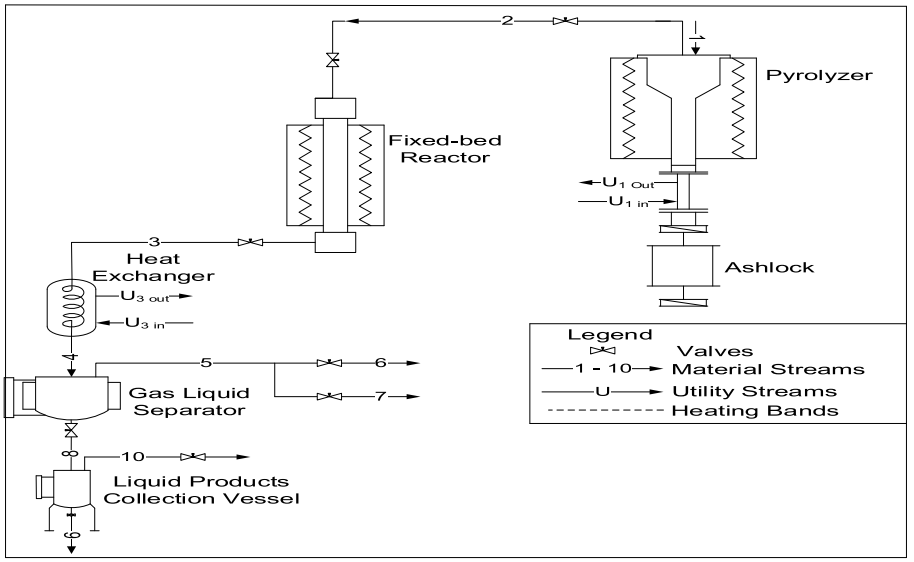

Figure 2. Process flow diagram for the pyrolysis process.

(Hubei Cubic-Ruiyi Instrument) for analysis. The experiment was also conducted using the same condition but without catalyst for comparison.

2.4. *Catalyst characterization*

Morphology of the samples was performed using a Phenom World scanning electron microscopy (SEM) analyzer (Thermo Fisher, Waltham, US). Infrared data was collected using a Shimadzu-8400S Fourier Transform Infrared Spectrometer (Kyoto, Japan) over the range of 4000–400 cm^{-1}. X-ray diffraction (XRD) measurements were conducted to determine the crystallinity of the sample using a Rigaku MiniFlex X-ray Diffractometer (Texas, USA) with 2θ between 2° and 80° while elemental composition was determined using a Genius IF Xenemetrix X-ray fluorescence (XRF) analyzer (Jordan Valley).

2.5. *Product characterization*

The composition of non-condensable products (gas) was measured using an online syngas analyzer (Hubei Cubic-Ruiyi Instrument). The functional groups in liquid products were determined using an attenuated total reflectance (ATR) mode of Shimadzu-8400S Fourier Transform Infrared Spectrometer (Kyoto, Japan) within the scan range of 600–4000 cm^{-1}. The composition of hydrocarbons in the liquid sample was determined using Agilent 19091S-433UI GCMS. Data was acquired using a 30 m × 250 μm × 0.25 μm capillary column flow rate of carrier gas (helium) set to 1.169 mL/min at a flow velocity of 39.404 cm/s. The initial column temperature was set to 50 °C and held for 5 min, and then ramped to 300 °C at 10 °C/min for 20 min. A sample volume of 1 μL was injected using the splitless injection mode at a temperature of 300 °C. The peaks of the resulting chromatographs were identified using the National Institute of Standards and Technology standard reference database.

3. Results and discussion

3.1. *Catalyst characterization*

3.1.1. *SEM analysis*

The size and morphology of the catalyst samples were analyzed using SEM analysis, and the results are shown in Figure 3. Alumina particles (Figure 3a) were irregular polyhedrons with angular shapes, which may improve permeability after sintering; see Kim et al. [34]. Both 3% FeO/Al and 5% FeO/Al catalysts exhibited a rough, flaky surface with irregularly shaped particles (Figures 3b,c), which were identified as mesoporous FeO deposited on the support after impregnation. The lighter regions in the images are composed primarily of the support while the

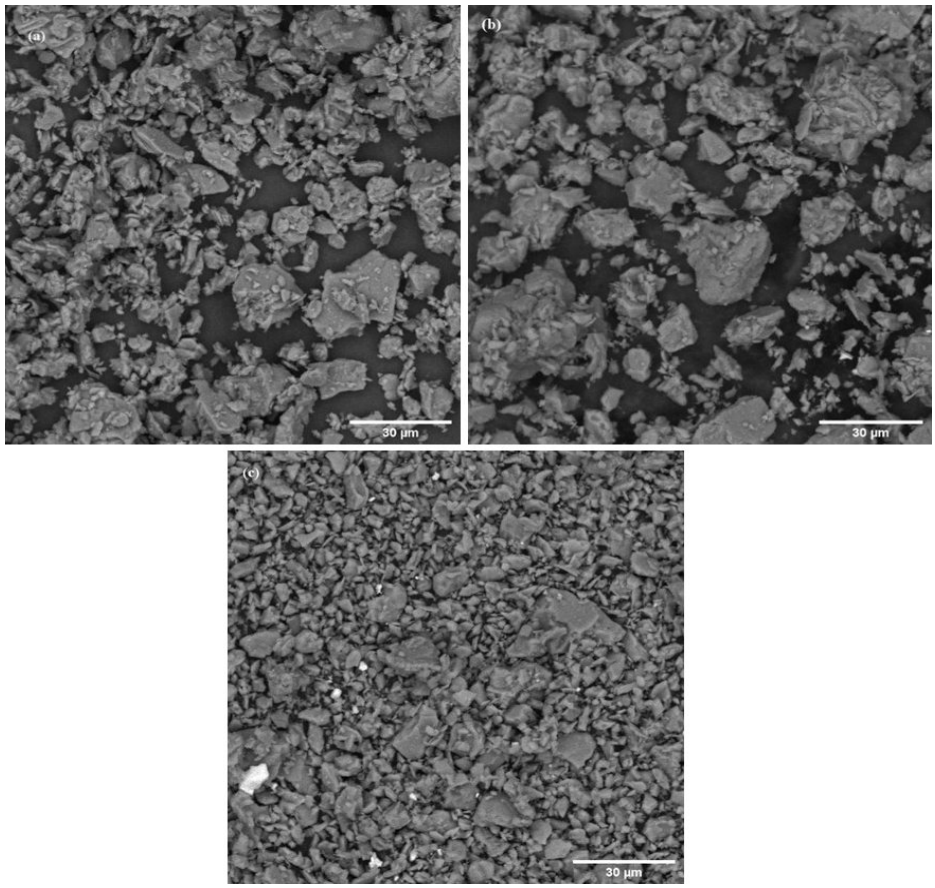

Figure 3. SEM micrograph at ×2000 of (a) alumina, (b) 3% FeO/Al, and (c) 5% FeO/Al.

darker regions are iron particles [29,35]. Additionally, the SEM images revealed many smaller particles dispersed on the surface of the support in 5% FeO/Al, indicating successful dispersion of the mesoporous FeO on the support. These observations confirm the successful synthesis of the catalyst as supported by similar finding in the literature [36].

The particle size analysis (Figure 4) revealed the presence of individual grains detectable at higher magnification (×2000) to be predominantly in the range of 1.42–7.63, 1.37–10.75, and 2.66–6.34 µm for alumina, 3% FeO/Al, and 5% FeO/Al, respectively. The average particle diameters were 4.45, 4.74, and 3.85 µm for alumina, 3% FeO/Al, and 5% FeO/Al, respectively. The smallest particle size was found in 5% FeO/Al. This suggests that impregnation with mesoporous FeO increased the surface area and therefore, could enhance the catalytic activity due to availability of more active sites for reaction.

3.1.2. *XRF analysis*

The metal compositions determined by XRF analysis of all the synthesized catalysts and supports are presented in Table 1. As shown in the table, the mesoporous FeO has been successfully incorporated onto the support, with the percentage compositions of Fe detected to be 3.43% and 4.74% for 3% and 5% FeO/Al catalysts, respectively, while Fe detected in alumina was just 0.11%. These compositions are comparable to the metal loadings in the calculation, suggesting that the synthesis process was effective. Moreover, the Al compositions were found to be 45.50%, 47.11%, and 47.90% for 5% FeO/Al, 3% FeO/Al, and alumina (the support), respectively, implying successful impregnation. Other elements were detected in negligible concentrations, signifying fewer impurities in the synthesized catalyst. These findings are consistent with the work

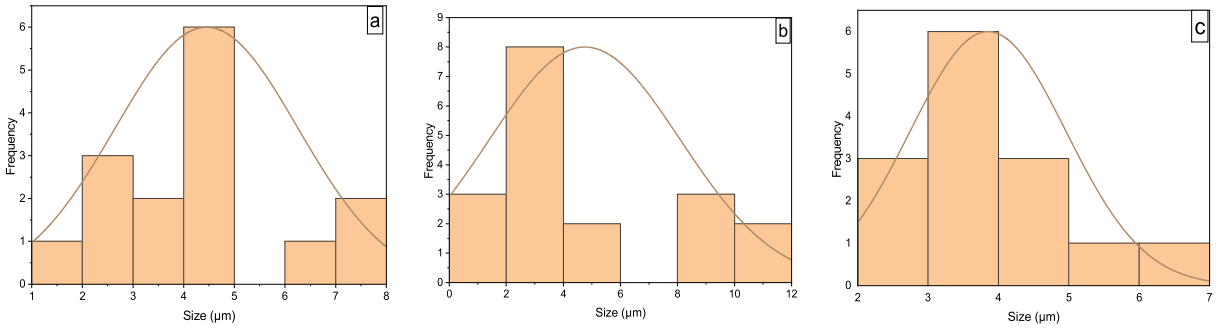

Figure 4. Histogram showing particle size distribution of (a) alumina, (b) 3% FeO/Al, and (c) 5% FeO/Al.

Table 1. Elemental compositions of 3% FeO/Al, 5% FeO/Al, and alumina

Elements	3% FeO/Al (%)	5% FeO/Al (%)	Alumina (%)
Si	1.36	1.52	1.35
AI	47.11	45.50	47.96
Fe	3.43	4.74	0.11
Ti	0.00	0.01	0.03
Ca	0.38	0.16	0.17
P	0.01	0.00	0.01
K	0.00	0.00	0.00
Mn	0.01	0.01	0.01
Mg	0.21	0.75	2.14
Zn	0.04	0.07	0.04

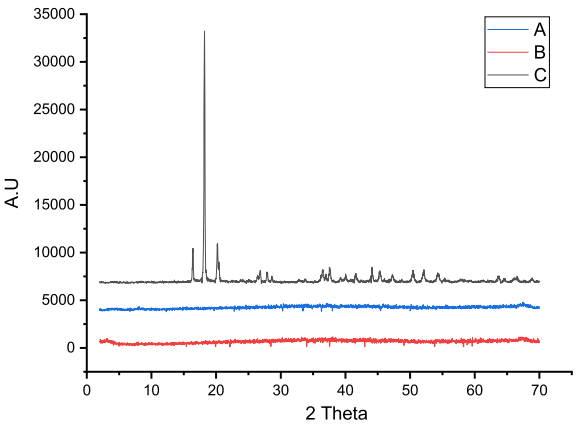

Figure 5. XRD pattern for (a) 3% FeO/Al, (b) 5% FeO/Al, and (c) alumina.

by Tanarungsun et al. [37], where Fe and other metals were impregnated onto TiO_2 support.

3.1.3. *XRD analysis*

The XRD patterns obtained for alumina (a), 3% FeO/Al (b), and 5% FeO/Al (c) are presented in Figure 5. It was observed that the pure alumina was the only crystalline phase identified by the International Centre for Diffraction Data (ICDD). However, the crystallinity of the synthesized catalyst samples was not detected, indicating that the catalyst is amorphous in nature. Amorphous catalysts have been shown to have higher surface areas, more active sites, and enhanced reactivity [38]. Several studies have reported similar results when iron oxide is doped on alumina. For instance, Ramdhani et al. [30], Zhong et al. [39], and Kamboj et al. [40] reported the absence of crystalline peaks after impregnation of alumina with iron oxide, suggesting the formation of an amorphous phase. The formation of a non-crystalline phase when FeO is impregnated on alumina could be because of high dispersion of Fe on the surface of the catalyst as reported in a previous study [30]. Another factor that could affect the crystallinity of the synthesized catalyst is the calcination temperature (450 °C). Several researchers have reported higher crystallinity for iron oxide doped on alumina at higher temperatures in the range of 500–1000 °C [39,41].

3.2. *Product analysis*

3.2.1. *Analysis of gaseous products*

Gaseous products were analyzed using an online gas analyzer after exposure to different catalysts.

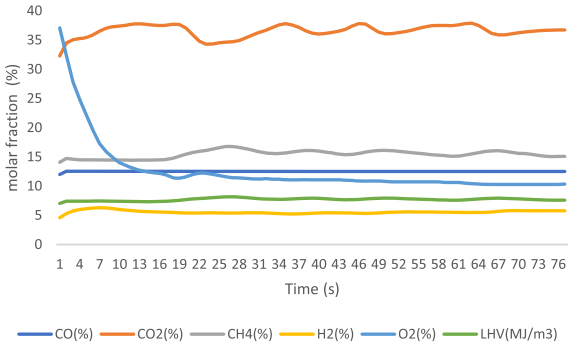

Figure 6. Gas analysis of reformed PET pyrolysis vapor using 3% Fe/Al catalyst.

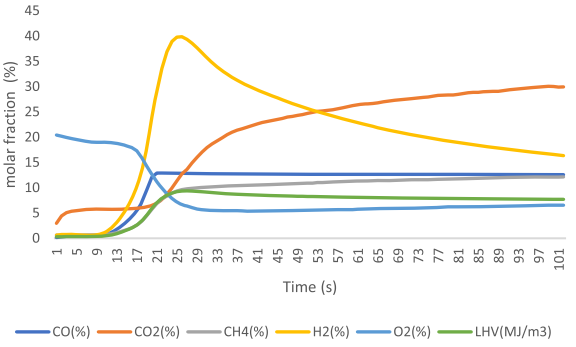

Figure 7. Gas analysis of reformed PET pyrolysis vapor using 5% Fe/Al catalyst.

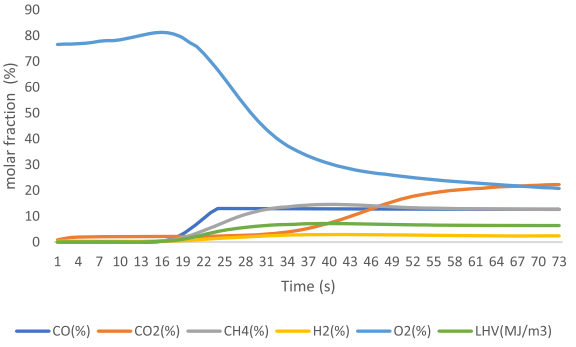

Figure 8. Gas analysis of pyrolysis vapor in blank run.

The obtained results are presented in Figures 6–8 for 3% FeO/Al, 5% FeO/Al, and blank run, respectively. The compositions of the components were reported when the readings from the analyzer stabilized, with values expressed as molar fractions in percentage (%). Oxygen content decreased from 23.3% in the blank run to 10.96% and 5.33% in 3% FeO/Al and 5% FeO/Al, respectively, indicating a decrease in oxygenated compounds when the synthesized catalyst was used. The H_2 content was highest in 5% FeO/Al, with a value of 17.14%. Conversely, the CH_4 content was highest in 3% FeO/Al (16.22%) and lowest in 5% FeO/Al (12.11%). The CO value decreased from 14.02% in the blank run to 12.51% and 12.64% in 3% FeO/Al and 5% FeO/Al, respectively, indicating an improvement in the synthesized catalyst. The CO_2 value was found to be 20.96%, 30.03%, and 36.86% for the blank run, 5% FeO/Al, and 3% FeO/Al, respectively. Furthermore, the low heating value was found to be 6.41, 7.72, and 7.84 MJ/m^3 for the blank run, 3% FeO/Al, and 5% FeO/Al, respectively. Similar findings was reported by Dhahak et al. [42] and Li et al. [43]. It is evident that the presence of the catalyst has improved the overall quality of the gas by reducing the O_2 content, and increasing the syngas (H_2/CO) and methane contents. These results demonstrated the effectiveness of the synthesized catalyst in reforming the pyrolysis gas.

3.2.2. *Analysis of liquid products*

Fourier transform infrared-ATR (FTIR-ATR) spectroscopy and gas chromatography mass spectrometry (GCMS) techniques were used to study the functional groups and hydrocarbon composition of the liquid products obtained before and after reforming using 3% and 5% FeO/Al catalysts. The FTIR spectra of the liquid product are shown in Figure 9 while the major functional groups are presented in Table 2 with their corresponding assignments. The results showed that the catalysts were able to reform PET vapor into aliphatic alkanes as can be seen by the presence of peaks at 2988 and 2899 cm^{-1}, which were absent in the blank run. Additionally, the peaks at 929, 1290, 1420, and 1689 cm^{-1} appeared to be more prominent in the reformed product using 5% FeO/Al catalyst, suggesting an increase in the quantity of aromatics. This underscores the excellent performance of the synthesized catalyst. A similar result has been reported in a previous study by Nasution et al. [44].

The analysis of liquid products by GCMS provided insight into the composition of hydrocarbons present with and without the catalyst. The composition of hydrocarbons present in the samples is summarized

Table 2. FTIR assignments for liquid products obtained for blank run and after catalytic reforming of pyrolysis vapor

Peaks (cm^{-1})	Blank run	3% FeO/Al	5% FeO/Al	Type of vibration	Nature of functional group
3050	✓	✓	✓	C–H stretching	Unsaturated aromatic
2924	×	✓	✓	C–H stretching	Aliphatic alkanes
2854	×	✓	✓	O–H stretching	Alcohols
1689	✓	✓	✓	C=O stretching	Alkenes
1420	✓	✓	✓	C–H stretching	Aromatic ring
1292	✓	✓	✓	C–H scissoring and bending	Alkene
1180	✓	✓	✓	C–O stretching	Alcohols, esters, carboxylic acids
923	✓	✓	✓	C–H bending	Alkene
713	✓	×	✓	C–H bending	Alkene, phenyl ring substitution
713	✓	✓	✓	C–H bending	Alkene, phenyl ring substitution

Key: ✓ = present, × = absent.

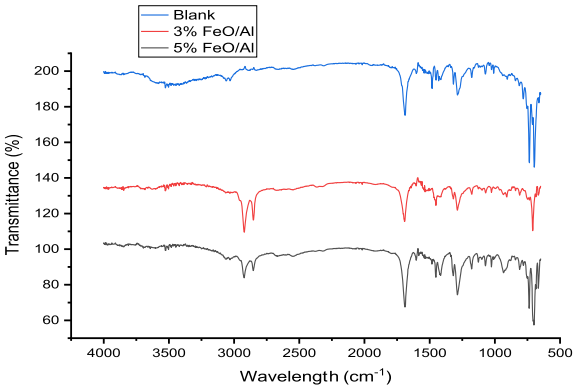

Figure 9. FTIR spectra of liquid product for blank run and after catalytic reforming of pyrolysis vapor.

in Table 3 while the GCMS chromatogram is presented in Figure 10. The results showed a significant change in hydrocarbon composition between the blank run and the reformed products. All the samples contained mixtures of aliphatic and aromatic hydrocarbons. However, increasing the percentage of mesoporous FeO impregnated in the catalyst (from 3% to 5% FeO) facilitated a selective catalytic reforming process as seen in the significant reduction of peaks from the blank run to that in the 5% FeO/Al sample. This led to a reduction in the formation of undesirable byproducts such as ketones, alcohols, esters, and acidic compounds, which were found in significant amounts in the blank run. These findings are in agreement with the work of Aisein et al. [45], Nasution et al. [44], and Rotta et al. [46]. Moreover, the data obtained substantiates the presence of aromatics and aliphatic hydrocarbons as inferred by the FTIR results. The findings indicated that the synthesized catalyst could transform complex pyrolysis vapor containing a wide range of products into a more streamlined composition of hydrocarbons. Similar results have been reported by Malik et al. [47].

4. Conclusion

This study investigated the pyrolysis of PET into fuel using synthesized mesoporous FeO-based catalysts (3% FeO/Al and 5% FeO/Al). Analyses using SEM, XRF, and XRD revealed the catalyst's well-defined morphological, structural, and compositional properties. Reforming using catalysts reduced oxygen content whereas CH_4 and H_2 contents were improved in the gaseous products. FTIR and GCMS analyses of liquid products demonstrated the catalyst's ability to reform pyrolysis vapor into valuable products.

These findings highlight the potential of mesoporous FeO-based catalysts in converting PET waste into valuable fuel products. This research contributes to the management of plastic waste by providing an alternative pathway for its conversion into useful products.

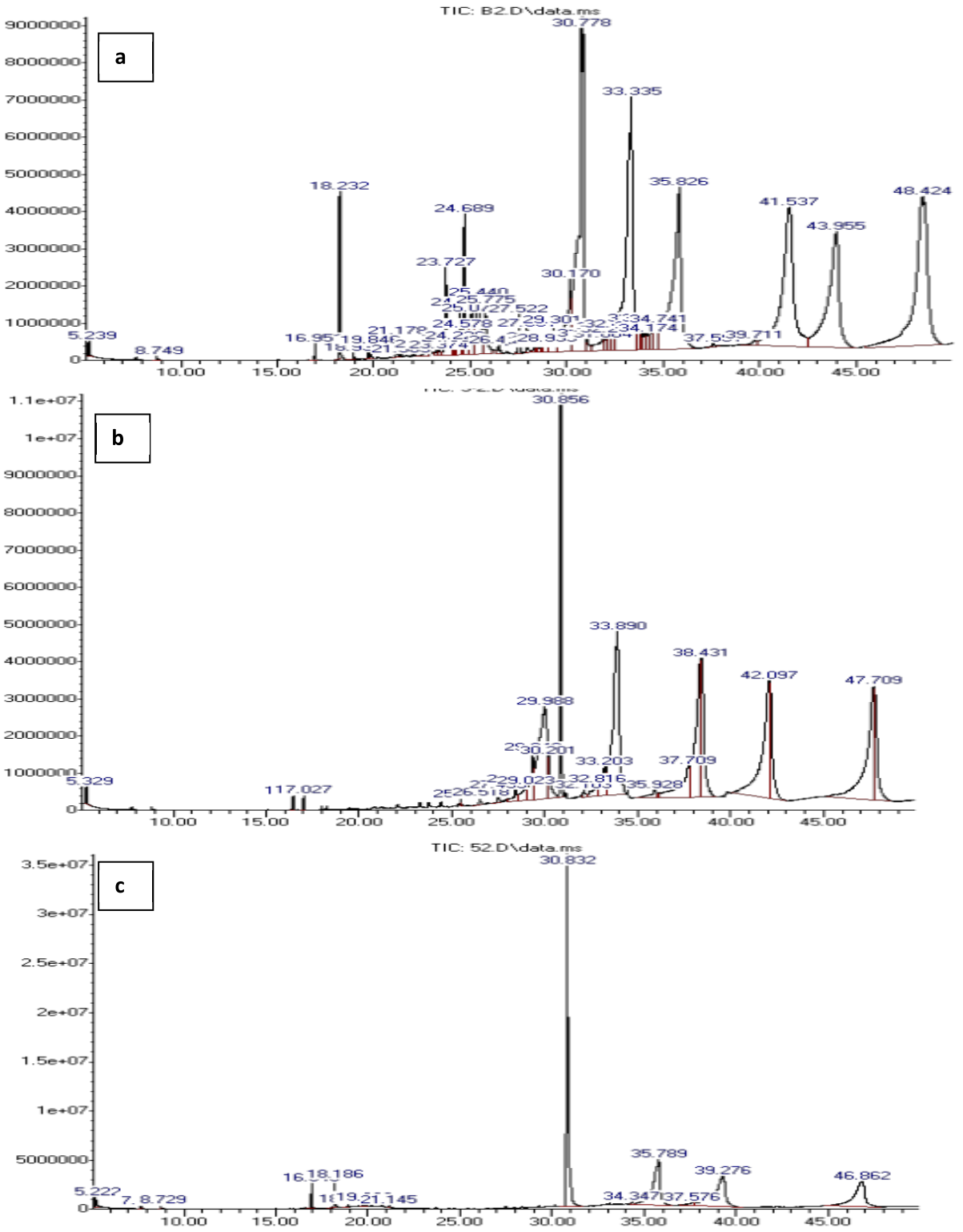

Figure 10. GCMS analysis of liquid products from catalytic reforming process (a) blank run, (b) 3% FeO/Al and (c) 5% FeO/Al.

Table 3. Composition of liquid product obtained for blank run and after catalytic reforming of pyrolysis vapor

Blank run	Relative area	3% FeO/Al	Relative area	5% FeO/Al	Relative area
Cyclohexane, methylene-	0.1244	Cycloeicosane	1.1838	Norbornane	0.5448
1,1'-Bicyclohexyl	0.1193	1-Chloroeicosane	2.1595	Benzene, chloro-	0.1316
Biphenyl	1.2557	Octadecane, 1-(ethenyloxy)-	11.0148	Cyclohexanol	0.1455
1,1'-Biphenyl, 3-methyl-	0.1059	Eicosane, 9-cyclohexyl-	1.2875	1,1'-Bicyclohexyl	1.2929
1,1'-Biphenyl, 4-methyl-	0.1236	Bis(2-ethylhexyl) phthalate	8.3623	Biphenyl	1.6627
Fluorene	0.2151	Octacosanal	0.9057	Fluorene, 2,4a-dihydro-	0.153
(E)-Stilbene	0.1875	Methoxyacetic acid, heptadecyl ester	1.7296	1,1'-Biphenyl, 4-methyl-	0.2786
9-Hexadecenoic acid	0.1144	9,12-Octadecadienoyl chloride, (Z,Z)-	15.3116	Fluorene	0.1634
Phenanthrene, tetradecahydro-	0.1218	Methoxyacetic acid, heptadecyl ester	4.1935	Diisooctyl phthalate	33.7527
Phenanthrene	1.4882	6-Nitroundec-5-ene	10.4797	Carbonic acid, octadecyl prop-1-en-2-yl ester	0.2488
2-Methyl-Z,Z-3,13-octadecadienol	0.1339	10-Methyl-E-11-tridece-1-ol acetate	6.2048	Octacosane	21.1329
9,12-Octadecadienoic acid (Z,Z)-	0.2398	9-Octadecynenitrile	12.0354	Erucic acid	1.0636
Naphthalene, 1-phenyl-	0.8766	7,11-Hexadecadienal	4.9289	9,12-Octadecadienoyl chloride, (Z,Z)-	21.1182
Anthracene, 1-methyl-	0.2604	9-Octadecenal	11.8024	9-Octadecenal	18.0856
o-Terphenyl	1.9577	9,12-Octadecadienoyl chloride, (Z,Z)-	5.6292	–	–
Phenanthrene, 4-methyl-	1.4162	–	–	–	–
Heptadecane	2.1588	–	–	–	–
Naphthalene, 2-phenyl-	1.1002	–	–	–	–
Heneicosane	0.1318	–	–	–	–
m-Terphenyl	0.4636	–	–	–	–
p-Terphenyl	0.2767	–	–	–	–
1-Chloroeicosane	0.1083	–	–	–	–

(continued on next page)

Table 3. (continued)

Blank run	Relative area	3% FeO/Al	Relative area	5% FeO/Al	Relative area
2-Propenoic acid, 2-cyano-3-(4-dimethylaminophenyl)-, ethyl ester	0.1069	–	–	–	–
Spiro[2.3]hexan-4-one, 5,5-diethyl-	0.1214	–	–	–	–
9,12-Octadecadienal	0.2133	–	–	–	–
1-Chloroeicosane	0.8156	–	–	–	–
Eicosane	3.0545	–	–	–	–
Diisooctyl phthalate	13.8353	–	–	–	–
Eicosane	0.2271	–	–	–	–
9-Methyl-10,12-hexadecadien-1-ol acetate	0.7105	–	–	–	–
Carbonic acid, eicosyl vinyl ester	0.31	–	–	–	–
Hexadecane, 1-(ethenyloxy)-	0.331	–	–	–	–
Hexadecane, 1-(ethenyloxy)-	0.5	–	–	–	–
Phthalic acid, isohexyl neopentyl ester	13.803	–	–	–	–
Bis-(3,5,5-trimethylhexyl) phthalate	0.4155	–	–	–	–
1,2-Benzenedicarboxylic acid, monobutyl ester	0.3703	–	–	–	–
Erucic acid	0.3204	–	–	–	–
Eicosane	0.5716	–	–	–	–
6-Nitroundec-5-ene	0.8206	–	–	–	–
Cycloeicosane	10.9885	–	–	–	–
Cycloeicosane	0.2487	–	–	–	–
9-Octadecenal	13.0695	–	–	–	–
9,12-Octadecadienal	10.4876	–	–	–	–
(Z)-1,3-Dimethoxypropan-2-yl docos-13-enoate	15.4166	–	–	–	–

Declaration of interests

The authors do not work for, advise, own shares in, or receive funds from any organization that could benefit from this article, and have declared no affiliations other than their research organizations.

Funding

The authors appreciate the NARICT for the financial and technical support rendered in carrying out this research under project number FGN/AB2021/ERGP30122610.

References

[1] U. N. P. Fund, *World Population Dashboard*, Saudi Arabia, 2022.

[2] T. Sogbanmu, *The Conversation*, 2022, Available from: https://theconversation.com/plastic-pollution-in-nigeria-is-poorly-studied-but-enough-is-known-to-urge-action-184591.

[3] T. Obiezu, *Nigerian Recyclers Reduce Plastic Waste By Exchanging Trash for Cash*, Voice of America, 2019, Retrieved March. Available from: https://www.voanews.com/africa/nigerian-recyclers-reduce-plastic-waste-exchanging-trash-cash#::text=Nigerian%20Recyclers%20Reduce%20Plastic%20Waste%20by%20Exchanging%20Trash%20for%20Cash,-By%20Timothy%20Obiezu&text=ABUJA%2C%20NIGERIA%20%2D%20Nigeria%20ge.

[4] O. A. Alabi, K. I. Ologbonjaye, O. Awosolu, O. E. Alalade, *J. Toxicol. Risk Assess.*, 2019, **5**, 1-13.

[5] R. Verma, K. Vinoda, M. Papireddy, A. Gowda, *Proc. Environ. Sci.*, 2016, **35**, 701-708.

[6] B. Yalwaji, H. O. John-Nwagwu, T. O. Sogbanmu, *Sci. Afr.*, 2022, **16**, article no. e01220.

[7] Y. Liu, W. Fu, T. Liu, Y. Zhang, B. Li, *J. Anal. Appl. Pyrol.*, 2022, **161**, article no. 105414.

[8] A. Brems, J. Baeyens, C. Vandecasteele, R. Dewil, *J. Air Waste Manag. Assoc.*, 2011, **61**, 721-731.

[9] J. Aguado, D. Serrano, G. San Miguel, J. Escola, J. Rodríguez, *J. Anal. Appl. Pyrol.*, 2007, **78**, 153-161.

[10] S. Al-Salem, A. Antelava, A. Constantinou, G. Manos, A. Dutta, *J. Environ. Manag.*, 2017, **197**, 177-198.

[11] N. Sakthipriya, *Sci. Total Environ.*, 2022, **809**, article no. 151160.

[12] A. T. Hoang, P. S. Varbanov, S. Nižetić, R. Sirohi, A. Pandey, R. Luque, K. H. Ng, *J. Cleaner Prod.*, 2022, **359**, article no. 131897.

[13] S. Kartik, H. K. Balsora, M. Sharma, A. Saptoro, R. K. Jain, J. B. Joshi, A. Sharma, *Therm. Sci. Eng. Prog.*, 2022, **32**, article no. 101316.

[14] K. Sivagami, K. V. Kumar, P. Tamizhdurai, D. Govindarajan, M. Kumar, I. Nambi, *RSC Adv.*, 2022, **12**, 7612-7620.

[15] M. H. Rahman, P. R. Bhoi, P. L. Menezes, *Renew. Sustain. Energy Rev.*, 2023, **188**, article no. 113799.

[16] A. Al-Rumaihi, M. Shahbaz, G. Mckay, H. Mackey, T. Al-Ansari, *Renew. Sustain. Energy Rev.*, 2022, **167**, article no. 112715.

[17] A. T. Hoang, H. C. Ong, I. R. Fattah, C. T. Chong, C. K. Cheng, R. Sakthivel, Y. S. Ok, *Fuel Process. Technol.*, 2021, **223**, article no. 106997.

[18] B. Adelawon, G. Latinwo, B. Eboibi, O. Agbede, S. Agarry, *Chem. Eng. Commun.*, 2022, **209**, 1246-1276.

[19] R. K. Mishra, K. Mohanty, *Liquid Biofuels: Fundamentals, Characterization, and Applications*, John Wiley & Sons, 2021, 231-284 pages.

[20] Y. Xue, P. Johnston, X. Bai, *Energy Convers. Manag.*, 2017, **142**, 441-451.

[21] S. Du, J. A. Valla, R. S. Parnas, G. M. Bollas, *ACS Sustain. Chem. Eng.*, 2016, **4**, 2852-2860.

[22] D. V. Suriapparao, D. A. Kumar, R. Vinu, *Sustain. Energy Technol. Assess.*, 2022, **49**, article no. 101781.

[23] W. Luo, Q. Hu, Z.-y. Fan *et al.*, *Energy*, 2020, **213**, article no. 119080.

[24] D. Serrano, J. Aguado, J. Escola, *Acs Catal.*, 2012, **2**, 1924-1941.

[25] T.-T. Meng, H. Zhang, F. Lü, L.-M. Shao, P.-J. He, *J. Anal. Appl. Pyrol.*, 2021, **159**, article no. 105312.

[26] J. Sun, J. Luo, J. Lin, R. Ma, S. Sun, L. Fang, H. Li, *Energy*, 2022, **247**, article no. 123547.

[27] N. Cai, S. Xia, X. Li *et al.*, *Waste Manag.*, 2021, **136**, 47-56.

[28] B. Ramadhani, T. Kivevele, J. H. Kihedu, Y. A. Jande, *Biomass Convers. Biorefin.*, 2020, **12**, 1369-1392.

[29] S. Mosallanejad, B. Z. Dlugogorski, E. M. Kennedy, M. Stockenhuber, *ACS Omega*, 2018, **3**, 5362-5374.

[30] E. P. Ramdhani, E. Santoso, H. Holilah *et al.*, *RSC Adv.*, 2023, **13**, 31989-31999.

[31] X. Shen, Z. Zhao, H. Li, X. Gao, X. Fan, *Mater. Today Chem.*, 2022, **26**, article no. 101166.

[32] N. Cai, X. Li, S. Xia *et al.*, *Energy Convers. Manag.*, 2021, **229**, article no. 113794.

[33] Z. S. Gano, E. A. Audu, A. A. Osigbesan, A. F. Ade-Ajayi, J. T. Barminas, *Inorg. Chem. Commun.*, 2024, **159**, article no. 111854.

[34] J. Kim, J.-H. Ha, J. Lee *et al.*, *J. Korean Ceram. Soc.*, 2017, **54**, 331-339.

[35] M. M. Mohamed, W. Bayoumy, H. El-Faramawy, W. El-Dogdog, A. A. Mohamed, *Renew. Energy*, 2020, **160**, 450-464.

[36] F. Gulshan, K. Okada, *J. Eng. Res.*, 2015, **3**, article no. 10.

[37] G. Tanarungsun, W. Kiatkittipong, P. Praserthdam, H. Yamada, T. Tagawa, S. Assabumrungrat, *J. Ind. Eng. Chem.*, 2008, **14**, 596-601.

[38] G. Chen, Y. Zhu, H. M. Chen *et al.*, *Adv. Mater.*, 2019, **31**, article no. 1900883.

[39] Z. Zhong, T. Prozorov, I. Felner, A. Gedanken, *J. Phys. Chem. B*, 1999, **103**, 947-956.

[40] N. Kamboj, A. S. Shamshirgar, E. V. Shirshneva-Vaschenko, I. Hussainova, *Mater. Chem. Phys.*, 2019, **225**, 340-346.

[41] A. O. Ali, A. M. El Naggar, A. S. Morshedy, W. A. Aboutaleb, N. H. Metwally, *Chemosphere*, 2022, **307**, article no. 136011.

[42] A. Dhahak, G. Hild, M. Rouaud, G. Mauviel, V. Burkle-Vitzthum, *J. Anal. Appl. Pyrol.*, 2019, **142**, article no. 104664.

[43] Y. Li, M. A. Nahil, P. T. Williams, *Chem. Eng. J.*, 2023, **467**, article no. 143427.

[44] F. Nasution, H. Husin, F. Abnisa, F. T. Yani, L. Maulinda, *Energy Convers. Manag.*, 2022, **273**, article no. 116440.

[45] F. A. Aisien, E. T. Aisien, *Sustain. Chem. Clim. Action*, 2023, **2**, article no. 100020.

[46] A. N. Rotta, C. Bota, B. Brem, D. I. Porumb, E. Gal, *Stud. Univ. Babes-Bolyai, Chem.*, 2022, **67**, 169-185.

[47] S. Malik, H. Gulab, K. Hussain, M. Hussain, M. Haleem, *Int. J. Environ. Sci. Technol.*, 2022, **19**, 4019-4036.